RESEARCH ARTICLE | FEBRUARY 18 2026

Thermal edge animation in a two-dimensional micro-cavity: Effect of nonuniform boundary smoothness in the entire range of gas rarefaction rates

S. Rafieenasab ; E. Roohi ; A. Manela

Physics of Fluids 38, 022013 (2026)
https://doi.org/10.1063/5.0313425

Physics of Fluids ARTICLE pubs.aip.org/aip/pof

Thermal edge animation in a two-dimensional micro-cavity: Effect of nonuniform boundary smoothness in the entire range of gas rarefaction rates

Cite as: Phys. Fluids **38**, 022013 (2026); doi: 10.1063/5.0313425
Submitted: 22 November 2025 · Accepted: 2 February 2026 ·
Published Online: 18 February 2026

S. Rafieenasab,[1] E. Roohi,[2] and A. Manela[3,a)]

AFFILIATIONS

[1]School of Mechanical and Aerospace Engineering, Gyeongsang National University, Jinju, Gyeongnam 52828, South Korea
[2]Mechanical and Industrial Engineering, University of Massachusetts Amherst, 160 Governors Dr., Amherst, Massachusetts 01003, USA
[3]The Stephen B. Klein Faculty of Aerospace Engineering, Technion Technion City, Haifa 3200003, Israel

[a)]**Author to whom correspondence should be addressed:** amanela@technion.ac.il

ABSTRACT

We study the steady gas flow generated in a micro-cavity through the coupling between all-imposed temperature differences and non-uniformity in surface smoothness. A two-dimensional square cavity is considered, where the boundary–gas interaction is modeled via the microscopic Maxwell condition. The upper cavity wall is diffuse reflecting and maintained at a uniform temperature. Its facing bottom surface is divided between fully specular and fully diffuse sections, where the latter is fixed at a temperature different from the upper wall. The side surfaces are fully specular, making the cavity enclosure equivalent to an infinite channel configuration with periodic diffuse-specular distribution of its bottom boundary. The problem is solved in the entire range of gas rarefaction rates, combining an analytical solution in the free-molecular limit with direct simulation Monte Carlo calculations at arbitrary Knudsen numbers. A pure conduction description is provided in the limit of vanishing rarefaction. The results indicate that, while the gas is stationary at free-molecular and continuum conditions, circular gas flow is generated in the near-free-molecular, intermediate and near-continuum regimes. The flow is induced by a thermal-edge-like effect, applied at the attachment between the specular and diffuse wall parts, where the non-uniformity in wall smoothness couples sharp temperature gradients. The forces on the cavity walls are calculated, suggesting the shear loading on the specular-diffuse surface as an indicator for the intensity of the thermal-edge effect in the cavity.

I. INTRODUCTION

The study of gas dynamics in micro- and nano-scale systems has become a cornerstone in modern engineering and applied physics. As the characteristic length and time scales reduce, non-continuum effects become significant, leading to the breakdown of the continuum hypothesis and the failure of the Navier–Stokes–Fourier description to predict the correct fluid behavior.[1–3] In the context of rarefied gas flows and their governing Boltzmann equation, the departure from continuum gives rise to a variety of non-intuitive physical phenomena. Among the most consequential of these are thermally induced flows, where gas motion is generated through surface temperature control, without the need for external pressure gradients or mechanical moving parts. This principle is fundamental to the operation of devices in vacuum technology, micro/nano-electro-mechanical systems (MEMS/NEMS), and low-density aerospace applications.

In the continuum flow regime, a temperature gradient applied to a stationary gas in a closed container may result in stationary heat conduction or natural convection (if external forces are present), yet does not induce a sustained, unidirectional flow along the boundaries. However, the interaction between gas molecules and solid surfaces at non-continuum conditions may convert thermal energy directly into kinetic energy of the bulk fluid. This phenomenon has been analyzed in a large number of works, revealing the known "ghost effect" and associated thermal creep mechanism, where a surface set at a given

temperature gradient induces gas flow from its colder to its hotter region.[4,5] First introduced by Maxwell, this observation has been followed and forms the basis of the renowned Knudsen pump.[6]

Over the past few decades, follow-up research has analyzed a broad range of related problems. Among these, the *thermal edge flow* considers the gas motion induced in the vicinity of a sharp edge of a heated or cooled surface, even where the surface is maintained isothermal.[7,8] The flow is driven by the large temperature gradients occurring in the edge-surrounding gas. Other related thermally induced motions include radiometric flow, which rationalizes the forces acting on the vanes of a Crookes radiometer,[9–12] thermal-stress slip flow,[13] and more complex higher-order effects such as nonlinear thermal stress flow.[14,15] Apart from the fundamental interest in examining the above, these flow mechanisms offer practical non-mechanical means for generating gas pumping, separation, and actuation at the micro-scale.

To advance current knowledge, it has recently been suggested that thermally induced flows may also be generated through modification of the surface structural smoothness rather than its temperature.[16] To illustrate the effect, the Maxwell boundary condition for gas-surface interaction has been considered, describing kinetic wall reflections as a combination of diffuse and specular scattering.[1] In diffuse reflection, molecules accommodate the wall properties at re-emission, whereas in specular reflection they rebound elastically with a reversed velocity component normal to the boundary. While no surface complies with either one of these descriptions, it is commonly accepted that realistic gas-surface interaction may be approximated via their linear superposition, governed by an empirically adjusted accommodation coefficient. Applying the Maxwell model, a recent study[16] demonstrated that a flow akin to thermal transpiration may be induced between parallel isothermal plates, fixed at uniform yet different temperatures, by creating a discontinuity in the accommodation coefficient along one of the walls. This spatial non-uniformity in surface smoothness induces a gradient in the gas temperature close to the junction, which, in turn, drives thermal edge flow. This approach appears attractive as a relative simple mechanism for generating bulk flow, as it obviates the need to maintain a temperature gradient within the solid material, which is a source of inefficiency and structural complexity.

Making use of the same geometry, Lotfian and Roohi[17,18] applied the specular-diffuse edge setup to consider its effectiveness on the separation of binary gas mixtures. Basing their analysis on direct simulation Monte Carlo (DSMC) calculations, it was demonstrated that species separation is indeed feasible, due to the mass difference between the mixture components and subsequent diffusion velocities in the flow field. A similar geometry was considered to study the flow developed in ratchet-like microchannels and other thermally driven flow configurations.[19–21]

While the computational investigation of wall-smoothness-induced thermal flow has provided valuable insights, a comprehensive analysis that bridges the entire range of gas rarefaction rates is still lacking. To this end, the present contribution analyses the thermally induced flow in a two-dimensional rectangular cavity with non-uniform wall accommodation distribution. An analytical solution is derived in the free-molecular limit, accompanied by DSMC calculations in the entire range of gas rarefaction rates. Closed-form expressions are found for the normal and shear forces on the cavity walls in the collisionless limit, and their variations with gas rarefaction are examined. In the continuum limit, the DSMC predictions are compared with the pure conduction solution expected at vanishing rarefaction. The analysis sheds light on the present thermal-edge flow mechanism, observed between near-free-molecular and continuum-limit flow conditions.

In Sec. II, the problem is stated. The free-molecular solution is derived in Sec. III, followed by description of the numerical DSMC scheme in Sec. IV. Our results are presented and discussed in Sec. V, and the work conclusions are outlined in Sec. VI. Technical details are relegated to the Appendix.

II. STATEMENT OF THE PROBLEM

Schematic of the problem is given in Fig. 1. Consider a stationary two-dimensional square cavity of side L^* filled with a perfect monatomic hard-sphere gas of total mass m^* per unit length (hereafter, asterisks denote dimensional quantities). The interaction between the solid cavity surfaces and the gas is modeled through the Maxwell boundary condition, combining diffuse and specular wall reflections.[1] Specifically, the cavity upper $y^* = L^*$ wall and $L - L_s^* < x < L^*$ part of its lower $y^* = 0^*$ surface are assumed diffuse reflecting with fixed temperatures, $T^* = T_u^*$ and $T^* = T_l^*$, respectively. All other boundaries, marked by the dashed lines, are fully specular. It is noted that, by using a different scattering rule, the gas behavior would differ from that predicted by the present model. This should be the case when imposing, for example, the Cercignani-Lampis-Lord interaction kernel,[22] as suggested in several contexts. In the following, we prefer model simplicity over a more involved treatment of the boundary interaction, that may only affect the results quantitatively but obviate analysis.

We seek to describe the flow field induced inside the cavity, generated by the interaction between the solid surfaces and the gas, in the whole range of gas rarefaction rates, from the free-molecular to the continuum limit regimes. In the framework of gas kinetic theory and the present two-dimensional steady-flow setup, the problem is governed by the velocity distribution function $f^* = f^*(x^*, y^*, \boldsymbol{\xi}^*)$ of finding a gas molecule at a position (x^*, y^*) with molecular velocity about

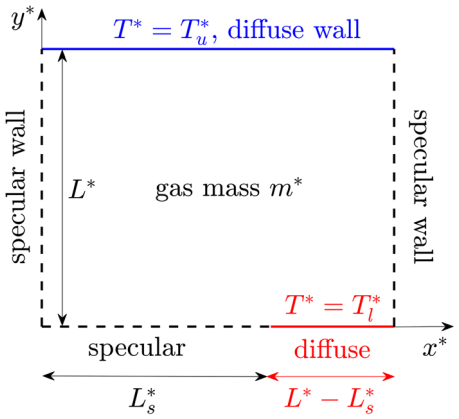

FIG. 1. Schematic of the problem. A two-dimensional square cavity of side L^* is filled with a perfect monatomic gas of total mass m^* per unit length. The cavity upper $y^* = L^*$ wall and $L - L_s^* < x < L^*$ part of its $y^* = 0^*$ surface are diffuse reflecting and fixed at temperatures $T^* = T_u^*$ and $T^* = T_l^*$, respectively. All other boundaries, marked by the dashed lines, are fully specular.

$\boldsymbol{\xi}^* = (\xi_x^*, \xi_y^*, \xi_z^*)$. In line with Fig. 1 and the above description, we impose the diffuse wall condition,

$$f^*\left(L_s^* < x^* < L^*, y^* = 0, \boldsymbol{\xi}^* \cdot \hat{\mathbf{n}} > 0\right) = \frac{\rho_l^*(x^*)}{\pi^{3/2} U_{\mathrm{mp}_h}^{*3}} \exp\left[-\frac{\xi^{*2}}{U_{\mathrm{mp}_h}^{*2}}\right]$$
$$\text{and } f^*(0 < x^* < L^*, y^* = L^*, \boldsymbol{\xi}^* \cdot \hat{\mathbf{n}} > 0) = \frac{\rho_u^*(x^*)}{\pi^{3/2} U_{\mathrm{mp}_c}^{*3}} \exp\left[-\frac{\xi^{*2}}{U_{\mathrm{mp}_c}^{*2}}\right], \tag{1}$$

over the $L_s^* < x^* < L^*$ part of the bottom wall and the entire upper surface, respectively, together with the specular wall reflection,

$$f^*(x_b^*, y_b^*, \boldsymbol{\xi}^* \cdot \hat{\mathbf{n}} > 0) = f^*(x_b^*, y_b^*, \boldsymbol{\xi}^* - 2(\boldsymbol{\xi}^* \cdot \hat{\mathbf{n}})\hat{\mathbf{n}}), \tag{2}$$

over the remaining boundaries, located along $0 < x_b^* < L_s^*$ with $y_b^* = 0$, $x_b^* = 0$ with $0 < y_b^* < L^*$, and $x_b^* = L^*$ with $0 < y_b^* < L^*$. In Eqs. (1) and (2), $\hat{\mathbf{n}}$ denotes a unit vector normal to the wall and into the cavity and $\rho_l^*(x^*)$ and $\rho_u^*(x^*)$ are yet unknown functions associated with the mass flux of particles reflected from the diffuse boundary. Additionally, $U_{\mathrm{mp}_l}^* = (2\mathcal{R}^* T_l^*)^{1/2}$ and $U_{\mathrm{mp}_u}^* = (2\mathcal{R}^* T_u^*)^{1/2}$ mark the most probable speeds of a gas particle at the diffuse lower and upper walls temperatures, respectively, where $\mathcal{R}^*$ denotes the specific gas constant.

To render the problem dimensionless, we scale the position by the cavity side length L^*, the velocity by the most probable molecular speed based on the upper wall temperature, $U_{\mathrm{mp}_u}^*$, the mass density by $\rho_0^* = m^*/L^{*2}$, and the temperature by T_u^*. The system non-dimensional description is then governed by

$$R_T = T_l^*/T_u^* \text{ and } L_s = L_s^*/L^*, \tag{3}$$

denoting the ratio between the diffuse lower and upper walls temperatures, and the relative size of the specular part of the lower surface, respectively. Additionally, the system state is determined by the value of the mean Knudsen number in the gas,

$$\mathrm{Kn} = \lambda^*/L^*, \tag{4}$$

where λ^* marks the mean free path of a particle. Assuming a variable-hard-sphere (VHS) model of interaction,[23] $\lambda^* = m_p^*/(2^{1/2}\pi\rho_0^* d^{*2})$, where m_p^* and d^* denote the gas single particle mass and effective diameter, respectively (see Sec. IV).

In what follows, we first analyze the free-molecular flow field in the cavity. No restrictions are made on the values of $R_T > 0$ and $0 \le L_s \le 1$, allowing for the inspection of the flow field at arbitrary temperature ratios and specular-diffuse divisions of the lower surface. The free-molecular analysis is followed by description of the DSMC scheme, to be applied at arbitrary Knudsen numbers.

III. THE FREE-MOLECULAR LIMIT

Assuming $\mathrm{Kn} \to \infty$, the non-dimensional kinetic problem is governed by the collisionless two-dimensional steady Boltzmann equation,

$$\xi_x \frac{\partial f}{\partial x} + \xi_y \frac{\partial f}{\partial y} = 0, \tag{5}$$

stating that $f(x, y, \boldsymbol{\xi})$ remains unchanged along "free-flight" particle trajectories in the absence of molecular collisions. Variations in the probability density function may therefore occur solely due to particle-surface interactions, prescribed by the scaled counterparts of Eq. (1),

$$f(L_s < x < 1, y = 0, \boldsymbol{\xi} \cdot \hat{\mathbf{n}} > 0) = \frac{\rho_l}{\pi^{3/2} R_T^{3/2}} \exp\left[-\frac{\xi^2}{R_T}\right]$$
$$\text{and } f(0 < x < 1, y = 1, \boldsymbol{\xi} \cdot \hat{\mathbf{n}} > 0) = \frac{\rho_u}{\pi^{3/2}} \exp\left[-\xi^2\right], \tag{6}$$

and Eq. (2),

$$f(x_b, y_b, \boldsymbol{\xi} \cdot \hat{\mathbf{n}} > 0) = f(x_b, y_b, \boldsymbol{\xi} - 2(\boldsymbol{\xi} \cdot \hat{\mathbf{n}})\hat{\mathbf{n}}). \tag{7}$$

While ρ_l and ρ_u in Eq. (6) are, in general, the functions of the coordinate x along the boundaries [cf. Eq. (1)], they may be treated as constants in the free-molecular limit, as justified below. We next derive a solution for the problem formulated in Eqs. (5)–(7).

In view of the collisionless regime and surface conditions considered, the velocity distribution function associated with each gas particle is determined through its most recent interaction with one of the cavity diffuse boundaries. It therefore equals to either the upper or lower wall Maxwellian distributions specified in Eq. (6). Noting the specular-wall type of the side $x = 0, 1$ boundaries, it is instructive to consider the equivalent infinite strip problem, obtained through the mirroring of the original cavity setup about its edge walls. This yields the configuration depicted in Fig. 2, where the strip is confined between an infinite upper $y = 1$ diffuse surface, held at a non-dimensional temperature $T = 1$, and a lower $y = 0$ wall, that is specular along $2n - L_s < x < 2n + L_s$, and diffuse, at a temperature $T = R_T$, along $2n + L_s < x < 2(n+1) - L_s$, where $n = 0, \pm 1, \pm 2, \ldots$. For clarity, the original cavity domain is highlighted in gray. Inspecting the setup in Fig. 2, the free-molecular problem satisfies the solution,

$$f(x, y, \boldsymbol{\xi}) = \begin{cases} \dfrac{\rho_u}{\pi^{3/2}} \exp\left[-\xi^2\right], & \xi_y < 0 \text{ or } \xi_y > 0 \text{ and } \dfrac{x - 2n - L_s}{y}\xi_y < \xi_x < \dfrac{x - 2n + L_s}{y}\xi_y, \\ \dfrac{\rho_l}{\pi^{3/2} R_T^{3/2}} \exp\left[-\dfrac{\xi^2}{R_T}\right], & \xi_y > 0 \text{ and } \dfrac{x - 2n - 2 + L_s}{y}\xi_y < \xi_x < \dfrac{x - 2n - L_s}{y}\xi_y, \end{cases} \tag{8}$$

where $n = 0, \pm 1, \pm 2, \ldots$, and the diffuse walls fluxes ρ_c and ρ_h are yet to be determined.

To fix ρ_u and ρ_l, we first impose the impermeability condition over the diffuse part of the cavity lower $y = 0$ boundary. Enforcing

$$\int_{-\infty}^{\infty} \xi_y f(1 - L_s < x < 1, y = 0, \boldsymbol{\xi}) \mathrm{d}\boldsymbol{\xi} = 0, \tag{9}$$

where $\mathrm{d}\boldsymbol{\xi} = \mathrm{d}\xi_x \mathrm{d}\xi_y \mathrm{d}\xi_z$, and substituting Eq. (8) into Eq. (9), we find

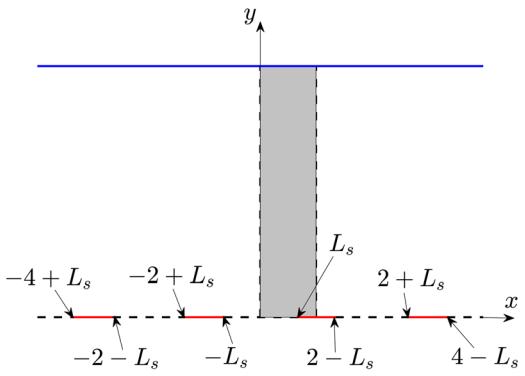

FIG. 2. Schematic of the equivalent infinite strip problem. The strip is confined between an upper $y = 1$ diffuse surface that is held at a non-dimensional temperature $T = 1$; and a lower $y = 0$ wall that is specular along its $2n - L_s < x < 2n + L_s$ sections, and diffuse with a temperature $T = R_T$ along its remaining $2n + L_s < x < 2(n + 1) - L_s$ parts, where $n = 0, \pm1, \pm2, \ldots$. The studied cavity domain (described in Fig. 1) is highlighted in gray.

$$\rho_u = \rho_l \sqrt{R_T}. \tag{10}$$

An identical expression is obtained by imposing the no-penetration condition over any of the other diffuse wall sections of the lower $y = 0$ surface, $2n + L_s < x < 2(n + 1) - L_s$ (with $n \neq 0$), as well as along the upper $y = 1$ wall. An additional constraint that fixes the values of ρ_u and ρ_l imposes the conservation of the total gas mass inside the cavity, namely,

$$\int_0^1 \int_0^1 \rho(x, y) \mathrm{d}x\mathrm{d}y = 1, \tag{11}$$

where $\rho(x, y)$ denotes the gas mass density. Having imposed Eq. (11), ρ_u and ρ_l are known, and the velocity distribution function $f(x, y, \boldsymbol{\xi})$ is determined.

Once the probability density function is calculated, the hydrodynamic fields are evaluated via appropriate quadratures over the molecular velocity space.[1] Specifically, the density ρ, x- and y-velocity components, and normal and shear stresses are given by

$$\begin{aligned}
\rho(x, y) &= \int_{-\infty}^{\infty} f \mathrm{d}\boldsymbol{\xi}, \quad u_x(x, y) = \frac{1}{\rho} \int_{-\infty}^{\infty} \xi_x f \mathrm{d}\boldsymbol{\xi}, \\
u_y(x, y) &= \frac{1}{\rho} \int_{-\infty}^{\infty} \xi_y f \mathrm{d}\boldsymbol{\xi}, \\
P_{xx}(x, y) &= \int_{-\infty}^{\infty} (\xi_x - u_x)^2 f \mathrm{d}\boldsymbol{\xi}, \\
P_{yy}(x, y) &= \int_{-\infty}^{\infty} (\xi_y - u_y)^2 f \mathrm{d}\boldsymbol{\xi}, \\
P_{zz}(x, y) &= \int_{-\infty}^{\infty} \xi_z^2 f \mathrm{d}\boldsymbol{\xi} \\
\text{and } P_{xy}(x, y) &= \int_{-\infty}^{\infty} (\xi_x - u_x)(\xi_y - u_y) f \mathrm{d}\boldsymbol{\xi},
\end{aligned} \tag{12}$$

respectively. Substituting Eq. (8) into Eq. (12) and integrating, the distribution of the macroscopic moments is obtained as specified in the Appendix. The pressure and temperature are consequently computed via $p = 2(P_{xx} + P_{yy} + P_{zz})/3$ and the scaled form of the ideal-gas equation of state, $T = p/\rho$, respectively.

IV. THE DSMC SCHEME

The DSMC method is the most commonly used scheme for simulating non-continuum gas flows. The method was initially introduced by Bird[23] to simulate the dynamics of a dilute gas, and was later on shown to yield results which converge to the solution of the Boltzmann equation.[24] Within the DSMC framework, the velocity distribution function of the gas molecules is represented by a number of computational particles. The computational domain is divided into a mesh of cells which size Δx^* is smaller than the particles' mean free path λ^*. Particles' motions and interactions are decoupled over a time step Δt^*, being shorter than the local mean free time τ^* between collisions. In each time step, the particles are first translated as if they do not interact with each other. Then, the particles are sorted into computational cells and collisions are evaluated stochastically, conserving the collision momentum and energy invariants. The computational cells are used for evaluating the macroscopic fields, which are obtained through weighted averages of the particles properties.

In the present work, we apply the DSMC algorithm to analyze the micro-cavity problem for arbitrary Knudsen numbers. The results obtained are used to validate the free-molecular solution, examine its breakdown with decreasing rarefaction, and study the system response in the intermediate and continuum flow regimes. We apply the no-time-counter (NTC) scheme[25] with the VHS model of molecular interactions,[23] where the effective molecular diameter d^* depends on the relative speed g^* between a pair of colliding particles,

$$d^*(g^*) = d^*_{\mathrm{ref}} \left(g^*_{\mathrm{ref}}/g^*\right)^{\omega - 1/2}.$$

Here, ω marks the viscosity ($\mu^* \propto T^{*\omega}$) and heat-conductivity ($\kappa^* \propto T^{*\omega}$) temperature power exponent, with $\omega = 0.74$ chosen to mimc air gas flow. In addition, $g^*_{\mathrm{ref}} = U^*_{\mathrm{mp}_u}$ is the reference relative speed and d^*_{ref} is the particle molecular diameter at the reference upper-wall temperature $T^* = T^*_u$. The two-dimensional computational domain was divided into cells of size $\Delta x^* \lesssim \lambda^*/3$, and the time step was set no larger than $\Delta t^* \approx \tau^*/5$. At the initial state, the simulation domain contained gas particles at uniform equilibrium with prescribed reference density and temperature. Then, at each time step, the particles free-flight motions and collisions were followed in accordance with the no-time counter scheme and VHS model. The diffuse or specular gas-wall interaction laws were applied to describe the scattering from the cavity boundaries, in accordance with the surface conditions specified in Fig. 1. The simulation was followed until a steady state was established, by letting the transient behavior evolve into a time-independent solution. The calculation of the macroscopic quantities commenced at steady state conditions, with the sampling time duration determined by requiring that the relative statistical error does not exceed 2% of the signal. The average number of particles per cell was taken ≈100, with most calculations through $\mathrm{Kn} \gtrsim 0.01$ lasting approximately 1 week using a multi-core Intel i7-4790K machine. At increasingly low Knudsen numbers, the calculated flow speed reduced considerably (vanishing at $\mathrm{Kn} \to 0$), and DSMC calculations become prohibitively expensive. Thus, for $O(10^{-3})$ low-Kn computations, a finer mesh was used, consisting of 2000 over 2000 cells with a total of 1.4×10^9 particles. To handle the computational workload in this case, the job was distributed across 150

processor cores and scheduled for a runtime of 14 days, ensuring sufficient data collection.

To verify the accuracy of results, a convergence analysis (not detailed here for brevity) was carried out. This has indicated that our simulation predictions are nearly unaffected by a further decrease in the above-mentioned cells size and time step, or by an increase in the number of particles taken per cell, thus ensuring the grid independence of the DSMC data.

V. RESULTS

In accordance with the statement of the problem in Sec. II, the non-dimensional problem is governed by the cavity reference Knudsen number Kn, the ratio R_T between the diffuse lower and upper wall temperatures, and the relative size L_s of the specular part of the lower surface. The limit cases of $L_s = 0$ and $L_s = 1$ correspond to the previously known one-dimensional setups of a gas at pure-conduction or uniform equilibrium states, respectively. To examine the two-dimensional problem, we therefore focus on a case where $L_s \neq 0, 1$, and vary the values of Kn and R_T. In Sec. V A, we fix $L_s = 0.65$ and $R_T = 3$ as a reference combination of parameters, and examine the effect of gas rarefaction, governed by the system Knudsen number, on the cavity flow field. In Sec. V B, we study the impact of varying the accommodation coefficient α along the left L_s part of the bottom surface, as well as the effects of varying the values of R_T, L_s and the gas models of intermolecular and surface interactions, on the results.

A. Reference case: L_s=0.65 and R_T=3

Figure 3 presents the effect of gas rarefaction on the temperature distribution in a cavity with the aforementioned $R_T = 3$ and $L_s = 0.65$ values. The figure shows the temperature-field colormaps at

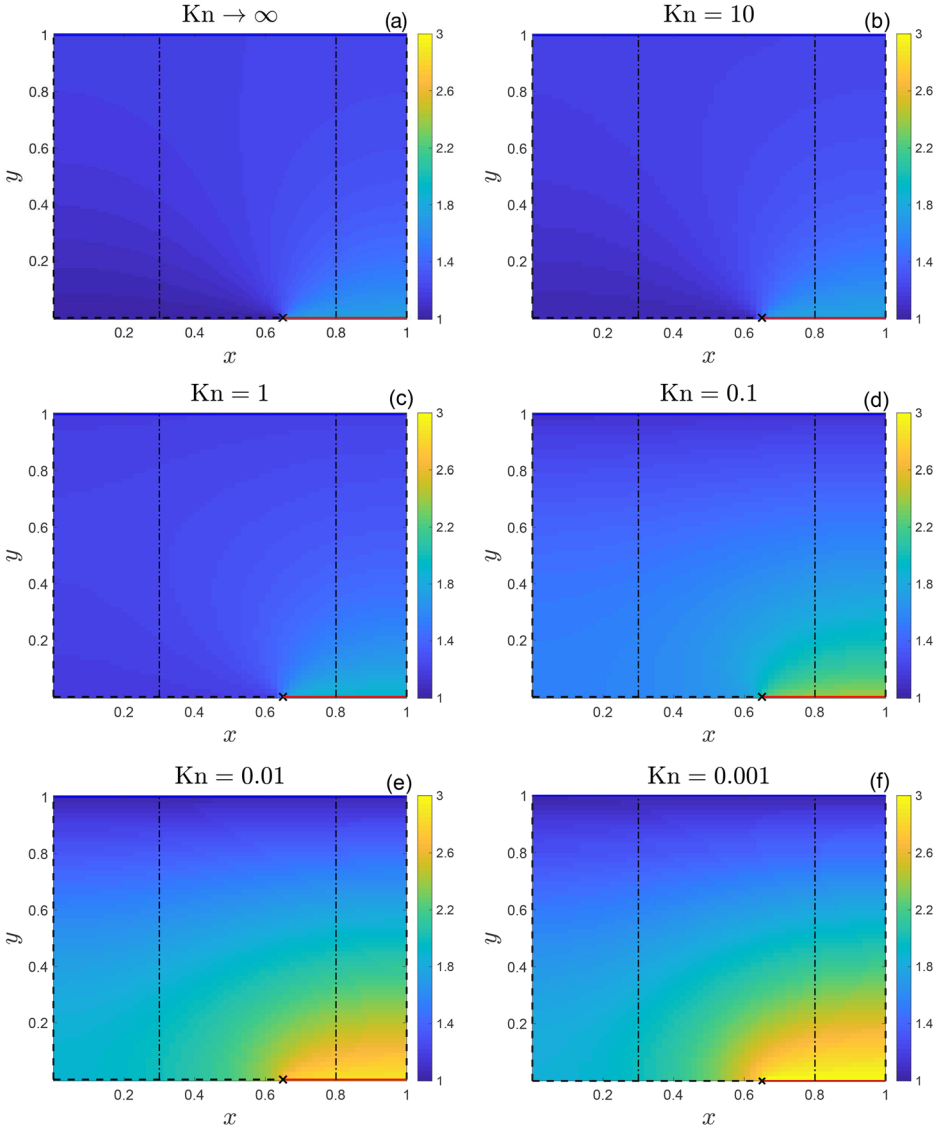

FIG. 3. Effect of gas rarefaction on the temperature distribution in a cavity with $R_T = 3$ and $L_s = 0.65$: colormaps of $T(x, y)$ at the indicated values of Kn. The crosses depict the location of the specular-diffuse junction along the lower wall [at $(x, y) = (L_s, 0)$], and the dash-dotted lines mark the $x = 0.3$ and $x = 0.8$ sections along which some of the results in Fig. 4 are presented.

the indicated values of Kn, where Fig. 3(a) depicts the free-molecular analytical solution and Figs. 3(b)–3(f) are based on DSMC calculations. The colorbar range of $1 \leq T \leq 3$ is kept identical in all parts for easy reference.

To start with, we note that the free-molecular field is nearly identical with the Kn = 10 result in Fig. 3(b). In both cases, the temperature ranges between $1 \lesssim T(x, y) \lesssim 1.75$, indicating a large temperature jump at the diffuse part of the lower plate surface, fixed at $T = R_T = 3$. With decreasing Kn, the temperature jump magnitude decreases and the field gradients in the vicinity of the specular-diffuse junction (which location is marked by the cross in each figure part) increase. At the lowest Kn = 0.001 value presented in Fig. 3(f), the temperature field becomes nearly identical with the diffuse walls, approaching $T = 1$ and $T = 3$ at the upper and lower-diffuse boundaries, respectively.

Based on the free-molecular solution in Sec. III and the calculation in the Appendix, the temperature distribution along the lower specular-diffuse wall is given by

$$T(x, y = 0; \mathrm{Kn} \to \infty) = \begin{cases} 1, & 0 < x < L_s, \\ \sqrt{R_T}, & L_s < x < 1, \end{cases} \tag{13}$$

in agreement with the $1 \lesssim T(x, y) \lesssim 1.75$ range observed in Figs. 3(a) and 3(b) for $R_T = 3$. To better validate this result, Fig. 4(a) shows the effect of the Knudsen number on the temperature distribution along the $y = 0$ lower boundary. The counterpart pressure distribution is presented in Fig. 4(b). Indeed, the DSMC result at Kn = 100 (marked by crosses) nearly coincides with the free-molecular distribution in Fig. 4(a), denoted by the blue line. With decreasing Kn, molecular collisions act to smoothen the wall-induced discontinuity and increase the overall gas temperature. The free-molecular description breaks

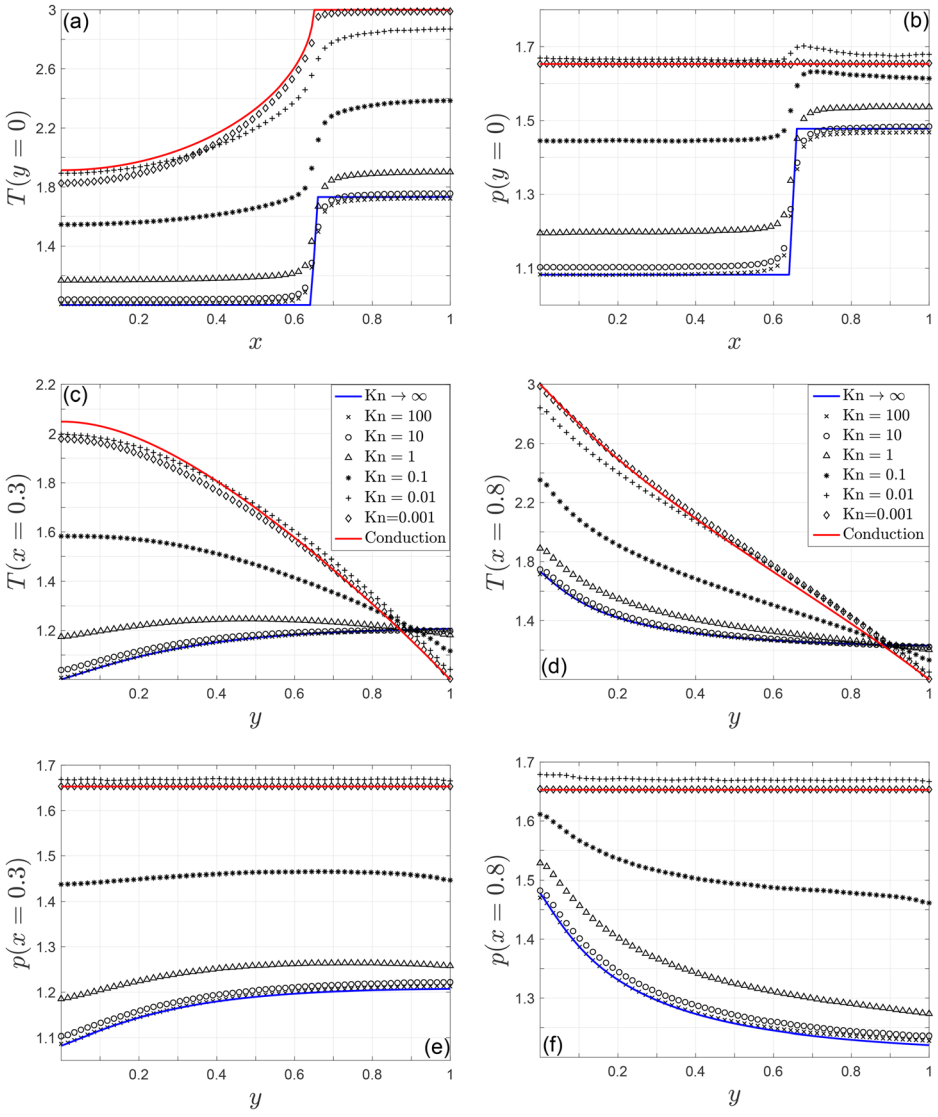

FIG. 4. Effect of gas rarefaction on the temperature (a), (c), and (d) and pressure (b), (e), and (f) distributions along $y = 0$ (a) and (b), $x = 0.3$ (c) and (e) and $x = 0.8$ (d) and (f). The symbols mark DSMC results at Kn = 100(×), 10 (°), 1 (△), 0.1 (∗), 0.01 (+), and 0.001 (◇). The blue and red curves denote the free-molecular and continuum pure conduction solutions, respectively.

down at $\mathrm{Kn} \lesssim 5$. At continuum-limit conditions, the temperature jump vanishes and the gas temperature at $y = 0$ along $L_S < x < 1$ nearly equals the surface temperature $R_T = 3$. Similar trends are observed in Figs. 4(c)–4(f), presenting the effect of the Knudsen number on temperature and pressure distributions along the $x = 0.3$ and $x = 0.8$ sections (cf. the dash-dotted lines in Fig. 3).

Assuming stationary-flow conditions at $\mathrm{Kn} \to 0$, the gas state in the continuum regime may be predicted based on the heat conduction equation and appropriate wall conditions. To this end, for the present VHS model of molecular interactions, the equation is given by

$$\nabla^2[T^{\omega+1}] = 0, \tag{14}$$

where $\nabla^2 = \partial^2/\partial x^2 + \partial^2/\partial y^2$ denotes the two-dimensional Laplacian operator and $\omega = 0.74$ (see Sec. IV). No jump and zero heat-flux boundary conditions are imposed at the cavity diffuse and specular walls, respectively. Specifically, along the lower and upper surfaces,

$$\left[\mathrm{H}(L_s - x)\frac{\partial T}{\partial y} + \mathrm{H}(x - L_s)T\right]_{y=0} = R_T \mathrm{H}(x - L_s) \text{ and } T(y = 1) = 1, \tag{15}$$

respectively, and over the side boundaries,

$$[\partial T/\partial x]_{x=0} = [\partial T/\partial x]_{x=1} = 0. \tag{16}$$

In Eq. (15), the Heaviside function notation $\mathrm{H}(\cdot)$ is used, to distinguish between the specular and diffuse parts of the wall. The Laplace-type problem formulated in Eqs. (14)–(16) is solved numerically using finite difference representations for the x-and y-derivatives. The results for the temperature, and then for the pressure [obtained through the equation of state and the imposition of the normalization condition in Eq. (11) for the density], are marked by the red curves in Fig. 4. The results closely match with the $\mathrm{Kn} = 0.001$ simulation data. In marked difference from the system state at highly rarefied conditions, the pressure field turns uniform in the continuum regime [see the red lines in Figs. 4(b), 4(e), and 4(f)]. This is in line with the respective momentum equation in the pure conduction state, requiring the vanishing of the pressure gradient.

While the gas in the cavity is stationary at free-molecular ($\mathrm{Kn} \to \infty$) and continuum ($\mathrm{Kn} \to 0$)conditions, flow animation is induced at finite Knudsen numbers. This is markedly different from the counterpart one-dimensional problem (with $L_s = 0$), where pure conduction prevails at all Knudsen numbers. To illustrate the two-dimensional flow field, Fig. 5 shows DSMC-calculated colormaps of the velocity magnitude and streamlines in the cavity in a sequence of finite decreasing Knudsen numbers. Circular counterclockwise flow is observed in all cases, in agreement with the cold-to-hot direction induced by the thermal edge effect along the wall (for $0 < R_T < 1$, where the upper wall temperature is higher than the lower, the flow direction is clockwise, as illustrated in Sec. V B). The flow speed maximizes close to the junction and reduces away from it. At the present choice of $L_s = 0.65$, stagnation is observed at $(x, y) \approx (0.55, 0.3)$, which is only slightly affected by the Knudsen number. Importantly, while the circular motion vanishes at exceedingly high and low rarefaction rates, it maximizes at $\mathrm{Kn} \sim O(10^{-1})$.

To quantify the non-monotonic variation of gas animation with the Knudsen number, Fig. 6(a) presents the effect of gas rarefaction on the total kinetic energy in the cavity, calculated via

$$E_k = \int_0^1 \int_0^1 \rho u^2 \mathrm{d}x\mathrm{d}y, \tag{17}$$

where $u = \sqrt{u_x^2 + u_y^2}$ denotes the macroscopic gas speed. In line with the results in Fig. 5, the system kinetic energy vanishes in both collisionless and continuum limits, and reaches a maximum at $\mathrm{Kn} \approx 0.07$. Importantly, non-zero kinetic energy levels are observed within $0.005 \lesssim \mathrm{Kn} \lesssim 5$, indicating that the thermal edge effect is non-negligible at near-free-molecular conditions. This suggests that the above free-molecular analysis may serve as a first step into asymptotic evaluation of the flow field at large yet finite Knudsen numbers. Such analysis, which may follow the scheme applied in other contexts (e.g., Ref. 26) is deferred to a later contribution.

We conclude the discussion of the reference case by analyzing the forces acting on the lower and upper cavity walls, normalized by $\rho_0 U_{\mathrm{mp}_u}^{*2} L^*$. To this end, the scaled normal forces over the lower and upper surfaces are given by

$$F_N^{(\mathrm{low})} = \int_0^1 P_{yy}(x, 0)\mathrm{d}x \text{ and } F_N^{(\mathrm{up})} = -\int_0^1 P_{yy}(x, 1)\mathrm{d}x, \tag{18}$$

respectively, and the counterpart shear forces are

$$F_S^{(\mathrm{low})} = -\int_0^1 P_{xy}(x, 0)\mathrm{d}x \text{ and } F_S^{(\mathrm{up})} = \int_0^1 P_{xy}(x, 1)\mathrm{d}x. \tag{19}$$

Applying the free-molecular analysis in Sec. III and in the Appendix, we find for the lower wall,

$$F_N^{(\mathrm{low})}(\mathrm{Kn} \to \infty) = -\frac{\rho_u}{4}(1 + L_s) - \frac{\rho_l R_T}{4}(1 - L_s) \text{ and } F_S^{(\mathrm{low})}(\mathrm{Kn} \to \infty) = 0. \tag{20}$$

Over the upper wall, the calculation involves summation over all contributions from the (equivalently infinite long) lower specular and diffuse surface segments (see Fig. 2 and the Appendix). For the normal force, this yields a value identical with the counterpart loading on the lower wall, namely,

$$F_N^{(\mathrm{up})}(\mathrm{Kn} \to \infty) = F_N^{(\mathrm{low})}(\mathrm{Kn} \to \infty). \tag{21}$$

For the shear force, we obtain

$$\begin{aligned} F_S^{(\mathrm{up})}&(\mathrm{Kn} \to \infty) \\ &= \frac{\rho_l R_T}{2\pi} \sum_{n=-\infty}^{\infty} \int_0^{\infty} s_y \mathrm{e}^{-s_y^2} \left\{ \exp\left[-(x + L_s - 2(n+1))^2 s_y^2\right] \right. \\ &\quad \left. - \exp\left[-(x - L_s - 2n)^2 s_y^2\right] \right\} \mathrm{d}s + \frac{\rho_u}{2\pi} \sum_{n=-\infty}^{\infty} \int_0^{\infty} \xi_y \mathrm{e}^{-\xi_y^2} \\ &\quad \times \left\{ \exp\left[-(x - L_s - 2n)^2 \xi_y^2\right] \right. \\ &\quad \left. - \exp\left[-(x + L_s - 2n)^2 \xi_y^2\right] \right\} \mathrm{d}\xi_y, \end{aligned} \tag{22}$$

which is evaluated numerically.

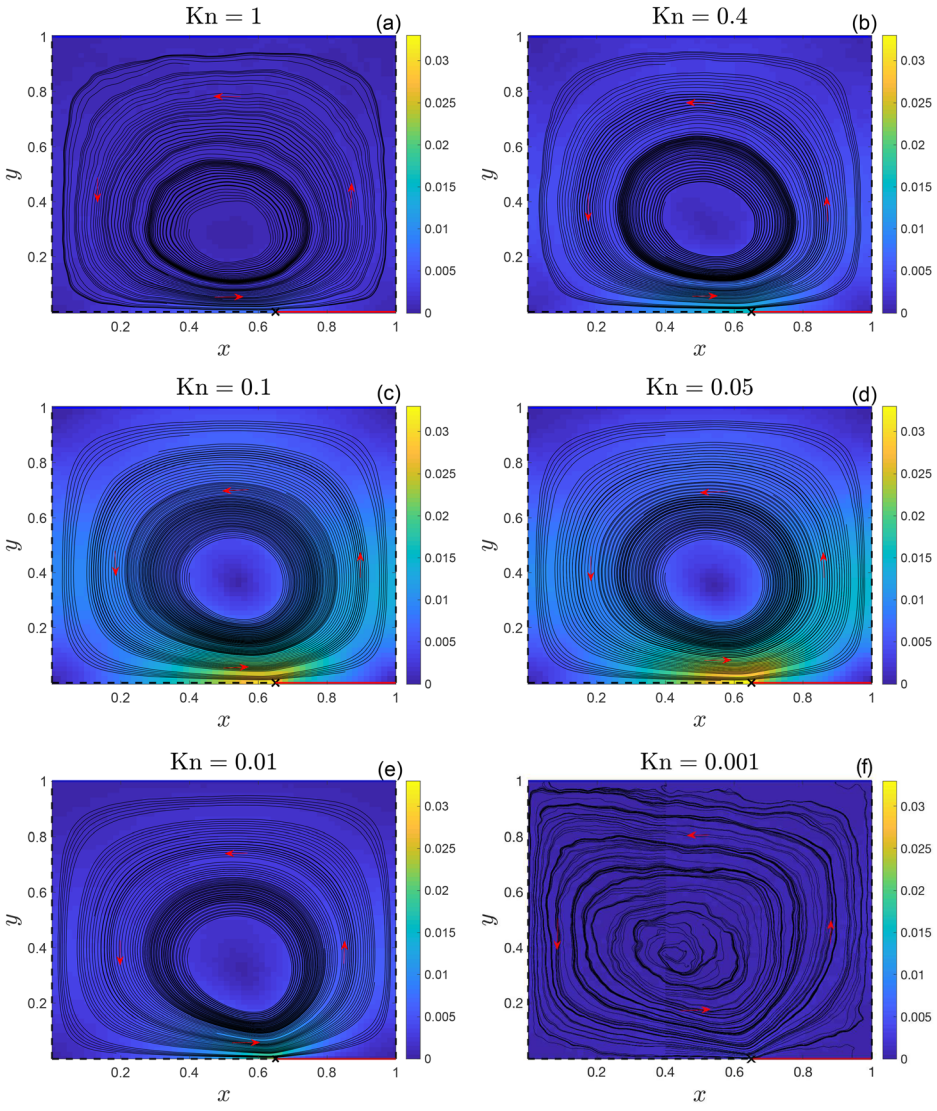

FIG. 5. Effect of gas rarefaction on the gas flow field in a cavity with $R_T = 3$ and $L_s = 0.65$: Colormaps of the DSMC-calculated velocity magnitude and flow streamlines at the indicated values of Kn. The crosses indicate the location of the specular-diffuse junction along the lower wall [at $(x, y) = (L_s, 0)$] and the red arrows mark the flow direction, which is counterclockwise in all cases.

Figures 6(b) and 6(c) show the variations with Kn of the normal [Fig. 6(b)] and shear [Fig. 6(c)] forces on the cavity upper and lower boundaries. The dashed lines in Figs. 6(b) and 6(c) show the analytical free-molecular predictions obtained in Eqs. (20)–(22), and the black and blue curves in Fig. 6(c) present the results for the lower and upper surfaces, respectively. The dash-dotted lines in Figs. 6(b) and 6(c) depict the force values obtained based on the pure conduction solution derived following Eqs. (14)–(16). At first, we observe that all asymptotes closely capture the limit values of the forces, supporting the accuracy of our analysis. The normal force common to both walls increases monotonically with decreasing Kn, growing by $\approx 30\%$ from its ballistic- to continuum-limit values. The shear force, however, varies qualitatively different. Being significantly lower in magnitude compared with the normal loading, it decreases with decreasing Kn over the upper wall, approaching $F_s = 0$ at $\mathrm{Kn} \to 0$. Markedly, the shear force over the lower surface varies non-monotonically with Kn, reaching a maximum at $\mathrm{Kn} \approx 0.07$. This is reminiscent of the value where maximum flow animation is observed in Fig. 6(a), suggesting the shear force over the specular-diffuse wall as an indicator for the intensity of the thermal-edge effect in the cavity.

B. Parametric study

To complement the above investigation on the impact of gas rarefaction, we study the effect of all other problem parameters on the cavity flow field. These include the impacts of the surface properties of the $0 < x < L_s$ part of the lower cavity wall, as well as the effects of varying the walls temperature ratio and the intermolecular interaction law.

To start with, Figs. 7(a) and 7(b) present the effect on the flow field of changing the Maxwell accommodation coefficient α along the $0 < x < L_s$ part of the bottom wall. In Fig. 7(a), $\alpha = 0.2$, and in Fig. 7(b), $\alpha = 0.6$. Keeping the same $L_s = 0.65$ and $R_T = 3$ values as in

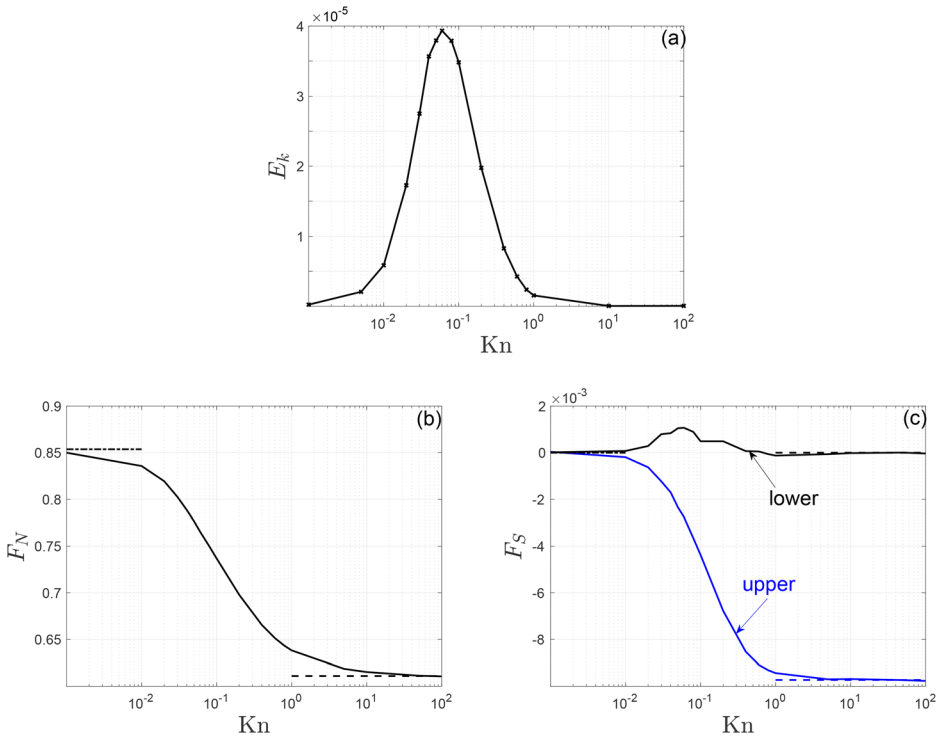

FIG. 6. Variations with Kn of the system total kinetic energy (a), and normal (b), and shear (c) forces on the cavity upper and lower boundaries. The dashed lines in (b) and (c) show the analytical free-molecular predictions, and the black and blue curves in (c) present the results for the lower and upper surfaces, respectively. The dash-dotted lines in (b) and (c) depict the force values obtained based on the pure conduction solution. All data presented correspond to a cavity with $R_T = 3$ and $L_s = 0.65$.

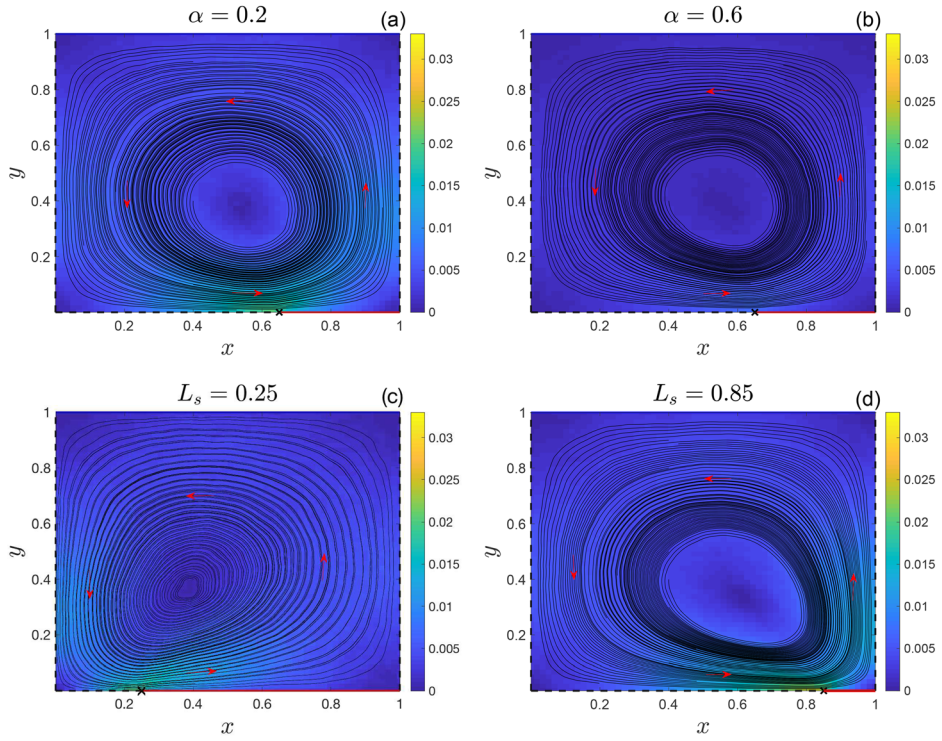

FIG. 7. Effects of the $0 < x < L_s$ bottom-wall-part Maxwell accommodation coefficient α (a) and (b) and size (c) and (d) on the gas flow field in a cavity with $R_T = 3$ and Kn $= 0.1$: colormaps of the DSMC-calculated velocity magnitude and flow streamlines for (a) and (b) $L_s = 0.65$ at $\alpha = 0.2$ (a) and $\alpha = 0.6$ (b), (c), and (d) $\alpha = 0$ with $L_s = 0.25$ (c) and $L_s = 0.85$ (d). The cross in each figure part indicates the location of the $x = L_s$ junction along the lower wall and the red arrows mark the flow direction, which is counterclockwise in all cases.

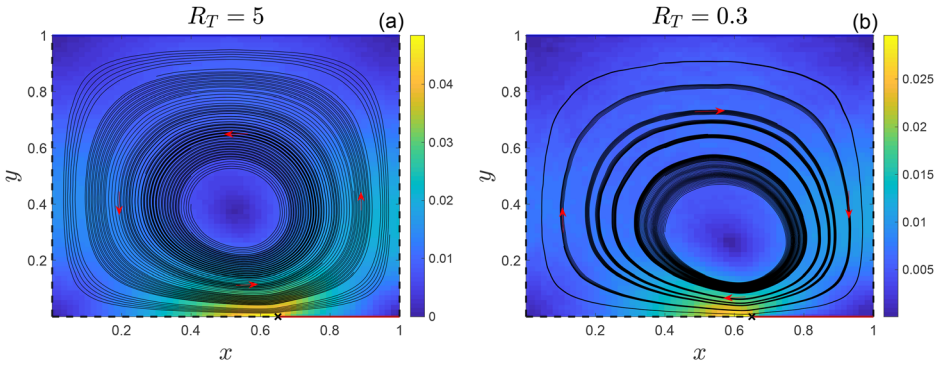

FIG. 8. Effect of the temperature ratio R_T on the gas flow field in a cavity with $L_s = 0.65$ and Kn $= 0.1$: colormaps of the DSMC-calculated velocity magnitude and flow streamlines at $R_T = 5$ (a) and $R_T = 0.3$ (b). The cross in each figure part indicates the location of the specular-diffuse junction along the lower wall, and the red arrows mark the flow direction, which is counterclockwise in (a) and clockwise in (b).

Sec. V A and fixing Kn $= 0.1$, the results are compared with the counterpart specular ($\alpha = 0$) case shown in Fig. 5(c). Using the same colorscale in all figures for easy reference, we find that the gas speed decreases with increasing α. This is since the change in wall smoothness imposed at the $x = L_s$ junction reduces with α, leading to a reduction in the thermal-edge effect. Quantitatively, in terms of the total gas kinetic energy in the cavity, our calculations indicate that $E_k \approx 3.5 \times 10^{-5}$ in the $\alpha = 0$ setup, while diminishing to $E_k \approx 1.7 \times 10^{-5}$ and $E_k \approx 2.8 \times 10^{-6}$ for $\alpha = 0.2$ and $\alpha = 0.6$, respectively. At $\alpha \to 1$, the bottom wall becomes uniformly diffuse, the problem turns one-dimensional, and a "pure conduction" state is established.

Inspecting the effect of the $0 < x < L_s$ bottom wall segment further, Figs. 7(c) and 7(d) show speed colormaps and velocity streamlines for the nominal specular-diffuse junction setup, yet with different values of L_s. In Fig. 7(c), $L_s = 0.25$ is taken, whereas $L_s = 0.85$ is considered in Fig. 7(d). Comparing again with Fig. 5(c), the results illustrate the distortion of the cavity flow field with varying L_s. Additionally, it is observed that the thermal edge effect reduces as L_s is taken closer to $L_s = 0$ and $L_s = 1$, for which the bottom wall becomes entirely diffuse or specular, respectively, and the problem degenerates into a one-dimensional configuration.

The effect of the temperature ratio R_T on the gas flow field is examined in Fig. 8. The figure shows velocity magnitude and streamline results for a cavity with $L_s = 0.65$ and Kn $= 0.1$, subject to $R_T = 5$ [in Fig. 8(a)] and $R_T = 0.3$ [in Fig. 8(b)] temperature ratios. Considering the result in Fig. 8(a) and comparing with Fig. 5(c), we note an increase in the gas speed with increasing $R_T > 1$, in line with the inevitably enhanced edge effect. In the $R_T = 0.3$ case shown in Fig. 8(b), where the bottom wall temperature is lower than the upper, we note that the flow direction is reversed and turns clockwise. This agrees with the expected edge-effect motion, inducing flow from the cold to the hot part of the bottom surface. An equivalent effect may be obtained by retaining $R_T > 1$ and interchanging between the specular and diffuse segment locations at the bottom wall, to be placed at $L_s < x < 1$ and $0 < x < L_s$, respectively.

Figure 9 presents the impacts of the gas-surface interaction and intermolecular models on the cavity flow field at the nominal $L_s = 0.65, R_T = 3$ and Kn $= 0.1$ choice of parameters. In Fig. 9(a), the VHS intermolecular interaction law is replaced by the variable-soft-sphere (VSS) model.[23] Using the same power exponent value for ω as in the VHS model, the comparison between Figs. 5(c) and 9(a) exhibits only slight quantitative difference, indicating that there is no qualitative effect in varying the molecular model of interaction. It is yet noted that the VSS-predicted velocity magnitude is slightly higher, in line with the softer scattering interaction and consequent reduced viscosity, allowing the transmission of a stronger edge effect. Proceeding to Fig. 9(b), we inspect the effect of replacing the specular wall condition along the $0 < x < L_s$ segment of the bottom wall with the

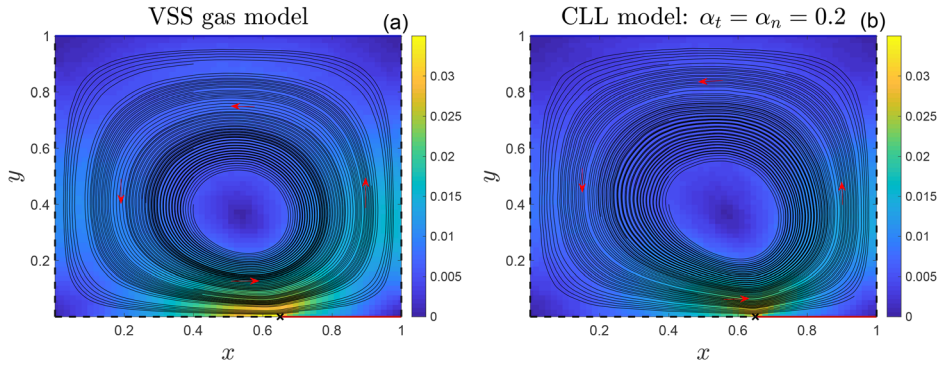

FIG. 9. Effects of the intermolecular interaction model (a) and the gas-surface interaction model (b) on the gas flow field in a cavity with $L_s = 0.65, R_T = 3$ and Kn $= 0.1$: colormaps of the DSMC-calculated velocity magnitude and flow streamlines for (a) a VSS gas in a specular-diffuse wall setup and (b) a VHS gas and CLL wall interaction along the $0 < x < L_s$ part of the bottom wall with $\alpha_t = \alpha_n = 0.2$. The cross in each figure part indicates the location of the $x = L_s$ junction along the lower wall and the red arrows mark the flow direction, which is counterclockwise in both (a) and (b).

Cercignani–Lampis–Lord interaction kernel.[22] Being governed by the tangential (α_t) and normal (α_n) accommodation coefficients, we set $\alpha_t = \alpha_n = 0.2$. This choice is intermediate between the specular ($\alpha_t = \alpha_n = 0$) and diffuse ($\alpha_t = \alpha_n = 1$) wall setups. The representative results Fig. 9(b) indicate that the effect is qualitatively similar to the one illustrated in Figs. 7(a) and 7(b): namely, that the "coarsening" of the $0 < x < L_s$ part of the bottom wall yields a reduction in the gradients induced at the $x = L_s$ junction point and a consequent decrease in the gas kinetic energy in the cavity. In this context, our current choice of the Maxwell condition prefers model simplicity over a more involved model, which enables the closed-form free-molecular-limit analysis carried in Sec. III.

To conclude, Fig. 10 examines the effect of the $0 < x < L_s$ bottom-wall-part Maxwell accommodation coefficient α and gas-surface interaction model on the temperature line distributions along $y = 0, x = 0.3$ and $x = 0.8$ for a cavity with $R_T = 3, L_s = 0.65$ and $\mathrm{Kn} = 0.1$. Specifically, the figure compares the specular-diffuse reference case (also presented in Fig. 4) with counterpart $\alpha = 0.2$ and $\alpha = 0.6$ setups, as well as with the result for the CLL interaction law for $\alpha_t = \alpha_n = 0.2$. All lines show similar trends, where the increase in the accommodation coefficient yields a general decrease in the temperature discontinuity along the $y = 0$ boundary, and an increase in the temperature inside the cavity. These are rationalized through the reduction in the thermal edge effect with increasing α. The CLL $\alpha_t = \alpha_n = 0.2$ result looks quantitatively similar to the $\alpha = 0.2$ case, supporting our application of the relatively simpler Maxwell model.

VI. CONCLUSIONS

We investigated the steady gas flow obtained in a micro-cavity through the coupling between wall-imposed temperature differences and non-uniformity in surface smoothness. A two-dimensional square cavity was considered, where the boundary-gas interaction was modeled via the microscopic Maxwell condition. Specifically, the upper cavity wall was assumed diffuse reflecting and maintained at a uniform temperature. Its facing bottom surface consisted of fully specular and fully diffuse sections, with the latter fixed at a temperature different from the upper wall. Taking the side solid walls as fully specular, the cavity enclosure was addressed equivalent to an infinite channel configuration with periodic diffuse-specular distribution of its bottom boundary. The problem was solved in the entire range of gas rarefaction rates, combining an analytical solution in the free-molecular limit with DSMC calculations at arbitrary Knudsen numbers. A pure conduction description was provided in the limit of vanishing rarefaction. The results indicate that, while the gas is stationary at free-molecular and continuum conditions, circular gas flow is generated in the near-free-molecular, intermediate and near-continuum regimes. The flow is induced by the thermal-edge effect, applied at the attachment between the specular and diffuse wall parts, where the non-uniformity in wall smoothness couples sharp temperature gradients. The forces on the cavity walls were calculated, suggesting the shear loading on the specular-diffuse wall as an indicator for the intensity of the thermal-edge effect in the cavity.

The thermal-edge phenomenon was studied previously in a set of works, focusing on the limit of small Knudsen numbers and deriving the corrections required in the traditional continuum-limit model to predict the observed system behavior.[1,7,8,14] Yet, the present occurrence of gas animation at relatively large $O(10^1)$ Knudsen numbers motivates a dedicated study of the problem at near-free-molecular conditions. For this purpose, the current free-molecular solution is suggested as a first step into asymptotic evaluation of the thermal-edge effect in the near-free-molecular and intermediate flow regimes. The analysis of this problem, where the thermally induced flow field may

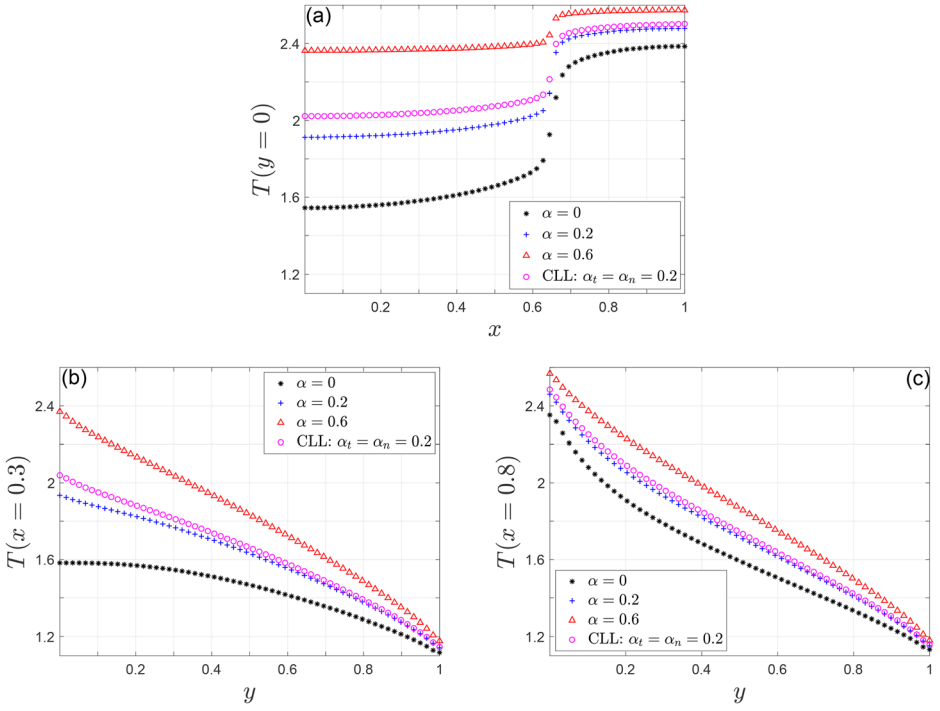

FIG. 10. Effect of the $0 < x < L_s$ bottom-wall-part Maxwell accommodation coefficient α and gas-surface interaction model on the temperature distribution along $y = 0$ (a), $x = 0.3$ (b) and $x = 0.8$ (c) for a cavity with $R_T = 3, L_s = 0.65$ and $\mathrm{Kn} = 0.1$. Each figure part compares between the nominal $\alpha = 0$ case ($*$) and $\alpha = 0.2$ ($+$, in blue), $\alpha = 0.6$ ($\triangle$, in red) and CLL model with $\alpha_t = \alpha_n = 0.2$ ($\circ$, in magenta).

be obtained as a first-order correction at large (yet finite) Knudsen numbers, is under way.

ACKNOWLEDGMENTS

A.M. acknowledges the support by the Israel Science Foundation (Grant No. 412/21).

AUTHOR DECLARATIONS

Conflict of Interest

The authors have no conflicts to disclose.

Author Contributions

S. Rafieenasab: Formal analysis (equal); Investigation (equal); Methodology (equal); Validation (equal). **E. Roohi:** Conceptualization (equal); Formal analysis (equal); Funding acquisition (equal); Investigation (equal); Methodology (equal); Software (equal); Supervision (equal); Validation (equal); Visualization (supporting); Writing – original draft (supporting); Writing – review & editing (supporting). **A. Manela:** Conceptualization (equal); Formal analysis (equal); Funding acquisition (equal); Investigation (equal); Methodology (equal); Software (equal); Validation (equal); Visualization (lead); Writing – original draft (lead); Writing – review & editing (equal).

DATA AVAILABILITY

The data that support the findings of this study are available from the corresponding author upon reasonable request.

APPENDIX: THE HYDRODYNAMIC FIELDS IN THE FREE-MOLECULAR LIMIT

In line with the problem analysis in Sec. III, each hydrodynamic field $G(x,y)$ may be expressed via the sum

$$G(x,y) = G^{(\mathrm{up})}(x,y) + G^{(\mathrm{low,diff})}(x,y) + G^{(\mathrm{low,spec})}(x,y), \tag{A1}$$

containing the contributions of particles arriving at (x,y) from the upper wall, $G^{(\mathrm{up})}$, and from the diffuse and specular sections of the lower wall, $G^{(\mathrm{low,diff})}$ and $G^{(\mathrm{low,spec})}$, respectively. Substituting Eq. (8) into Eq. (12), all ξ_z quadratures may be carried out analytically. Additionally, the integrations over the lower surface are expressed, as formulated below, via separate sums over the diffuse and specular parts.

Starting with the density, we find for the contribution of particles arriving from the upper wall,

$$\rho^{(\mathrm{up})}(x,y) = \rho_u/2. \tag{A2}$$

For the contribution of the particles from the diffuse sections of the lower surface, we carry out the change of variables $s_y = \xi_y/\sqrt{R_T}$, yielding, after ξ_z and ξ_x integrations,

$$\rho^{(\mathrm{low,diff})}(x,y) = \frac{\rho_l}{2\sqrt{\pi}} \sum_{n=-\infty}^{\infty} \int_0^{\infty} \mathrm{e}^{-s_y^2} \left[\mathrm{erfc}\left(\frac{x-2(n+1)+L_s}{y} s_y \right) - \mathrm{erfc}\left(\frac{x-2n-L_s}{y} s_y \right) \right] \mathrm{d}s_y, \tag{A3}$$

where

$$\mathrm{erfc}(p) \equiv \frac{2}{\sqrt{\pi}} \int_p^{\infty} \exp\left[-q^2\right] \mathrm{d}q$$

marks the Complementary Error function. The contribution of the particles arriving from the specular sections of the lower surface is

$$\rho^{(\mathrm{low,spec})}(x,y) = \frac{\rho_u}{2\sqrt{\pi}} \sum_{n=-\infty}^{\infty} \int_0^{\infty} \mathrm{e}^{-\xi_y^2} \left[\mathrm{erfc}\left(\frac{x-2n-L_s}{y} \xi_y \right) - \mathrm{erfc}\left(\frac{x-2n+L_s}{y} \xi_y \right) \right] \mathrm{d}\xi_y. \tag{A4}$$

In accordance with Eq. (A1), the total hydrodynamic density $\rho = \rho(x,y)$ is then given by the sum of Eqs. (A2)–(A4).

Proceeding to higher-order moments, the calculation of the x and y free-molecular velocity components is skipped, as the velocity field vanishes in the collisionless limit. To obtain the normal stress components, we substitute Eq. (8) into $P_{ii}(x,y)$ in Eq. (12) with $u_x = u_y = 0$. For P_{xx}, the calculation yields

$$P_{xx}^{(\mathrm{up})}(x,y) = \rho_u/4, \tag{A5}$$

$$P_{xx}^{(\mathrm{low,diff})}(x,y) = \frac{\rho_l R_T}{\pi} \sum_{n=-\infty}^{\infty} \int_0^{\infty} \mathrm{e}^{-s_y^2} \left\{ \frac{x-2(n+1)+L_s}{2y} s_y \exp\left[\frac{(x-2(n+1)+L_s)^2}{y^2} s_y^2 \right] - \frac{(x-2n-L_s)}{2y} s_y \exp\left[\frac{(x-2n-L_s)^2}{y^2} s_y^2 \right] + \frac{\sqrt{\pi}}{4} \left[\mathrm{erfc}\left(\frac{x-2(n+1)+L_s}{y} s_y \right) - \mathrm{erfc}\left(\frac{x-2n-L_s}{y} s_y \right) \right] \right\} \mathrm{d}s_y, \tag{A6}$$

and

$$P_{xx}^{(\mathrm{low,spec})}(x,y) = \frac{\rho_u}{\pi} \sum_{n=-\infty}^{\infty} \int_0^{\infty} \mathrm{e}^{-\xi_y^2} \left\{ \frac{(x-2n-L_s)}{2y} \xi_y \exp\left[\frac{(x-2n-L_s)^2}{y^2} \xi_y^2 \right] - \frac{(x-2n+L_s)}{2y} \xi_y \exp\left[\frac{(x-2n+L_s)^2}{y^2} \xi_y^2 \right] + \frac{\sqrt{\pi}}{4} \left[\mathrm{erfc}\left(\frac{x-2n-L_s}{y} \xi_y \right) - \mathrm{erfc}\left(\frac{x-2n+L_s}{y} \xi_y \right) \right] \right\} \mathrm{d}\xi_y, \tag{A7}$$

whereas for P_{yy} we obtain

$$P_{yy}^{(\mathrm{up})}(x,y) = \rho_u/4, \tag{A8}$$

$$P_{yy}^{(\mathrm{low,diff})}(x,y) = \frac{\rho_l R_T}{2\sqrt{\pi}} \sum_{n=-\infty}^{\infty} \int_0^{\infty} s_y^2 \mathrm{e}^{-s_y^2} \times \left[\mathrm{erfc}\left(\frac{x-2(n+1)+L_s}{y} s_y \right) - \mathrm{erfc}\left(\frac{x-2n-L_s}{y} s_y \right) \right] \mathrm{d}s_y, \tag{A9}$$

and

$$P_{yy}^{(\mathrm{low,spec})}(x,y) = \frac{\rho_u}{\pi} \sum_{n=-\infty}^{\infty} \int_0^{\infty} \mathrm{e}^{-\xi_y^2} \left\{ \frac{(x-2n-L_s)}{2y} \xi_y \times \exp\left[\frac{(x-2n-L_s)^2}{y^2} \xi_y^2 \right] - \frac{(x-2n+L_s)}{2y} \xi_y \times \exp\left[\frac{(x-2n+L_s)^2}{y^2} \xi_y^2 \right] + \frac{\sqrt{\pi}}{4} \left[\mathrm{erfc}\left(\frac{x-2n-L_s}{y} \xi_y \right) - \mathrm{erfc}\left(\frac{x-2n+L_s}{y} \xi_y \right) \right] \right\} \mathrm{d}\xi_y. \tag{A10}$$

The total P_{xx} and P_{yy} distributions are given by the sums of Eqs. (A5)–(A10), respectively. For P_{zz}, the expression simplifies to

$$P_{zz}(x,y) = \frac{\rho_u}{4} + \frac{R_T}{2} \rho^{(\mathrm{low,diff})}(x,y) + \frac{1}{2} \rho^{(\mathrm{low,spec})}(x,y). \tag{A11}$$

The free-molecular gas pressure and temperature are given by $p = 2(P_{xx} + P_{yy} + P_{zz})/3$ and $T = p/\rho$, respectively, as noted after Eq. (12).

REFERENCES

[1] Y. Sone, *Molecular Gas Dynamics: Theory, Techniques, and Applications* (Birkhäuser, Boston, 2007).
[2] G. A. Bird, *Molecular Gas Dynamics and the Direct Simulation of Gas Flows* (Oxford University Press, Oxford, UK, 1994).
[3] E. Roohi, H. Akhlaghi, and S. Stefanov, *Advances in Direct Simulation Monte Carlo: From Micro-Scale to Rarefied Flow Phenomena* (Springer Nature, Singapore, 2025).
[4] Y. Sone, "Thermal creep in rarefied gas," J. Phys. Soc. Jpn. **21**, 1836–1837 (1966).
[5] T. Ohwada, Y. Sone, and K. Aoki, "Numerical analysis of the shear and thermal creep flows of a rarefied gas over a plane wall on the basis of the linearized Boltzmann equation for hard-sphere molecules," Phys. Fluids A **1**, 1588–1599 (1989).
[6] M. Knudsen, "Eine revision der gleichgewichtsbedingung der gase. thermische molekularströmung," Ann. Phys. **336**, 205–229 (1909).
[7] Y. Sone and M. Yoshimoto, "Demonstration of a rarefied gas flow induced near the edge of a uniformly heated plate," Phys. Fluids **9**, 3530–3534 (1997).
[8] K. Aoki, Y. Sone, and Y. Waniguchi, "A rarefied gas flow induced by a temperature field: Numerical analysis of the flow between two coaxial elliptic cylinders with different uniform temperatures," Comput. Math. Appl. **35**, 15–28 (1998).
[9] S. Taguchi and K. Aoki, "Motion of an array of plates in a rarefied gas caused by radiometric force," Phys. Rev. E **91**, 063007 (2015).
[10] V. Shahabi, T. Baier, E. Roohi, and S. Hardt, "Thermally induced gas flows in ratchet channels with diffuse and specular boundaries," Sci. Rep. **7**, 41412 (2017).
[11] A. Lotfian and E. Roohi, "Radiometric flow in periodically patterned channels: Fluid physics and improved configurations," J. Fluid Mech. **860**, 544–576 (2019).
[12] H. Akhlaghi, E. Roohi, and S. Stefanov, "A comprehensive review on micro-and nano-scale gas flow effects: Slip-jump phenomena, Knudsen paradox, thermally-driven flows, and Knudsen pumps," Phys. Rep. **997**, 1–60 (2023).
[13] Y. Sone and S. Tanaka, "Thermal stress slip flow induced in rarefied gas between noncoaxial circular cylinders, Memoirs of the Faculty of Engineering," Kyoto Univ. **43**, 344–363 (1981).
[14] Y. Sone, "Flows induced by temperature fields in a rarefied gas and their ghost effect on the behavior of a gas in the continuum limit," Annu. Rev. Fluid Mech. **32**, 779–811 (2000).
[15] M. Mousivand and E. Roohi, "On the nonlinear thermal stress, thermal creep, and thermal edge flows in triangular cavities," Phys. Fluids **34**, 052002 (2022).
[16] S. Sugimoto and H. Sugimoto, "Thermal transpiration flows induced by differences in accommodation coefficients," Phys. Fluids **34**, 042005 (2022).
[17] A. Lotfian and E. Roohi, "Binary gas mixtures separation using microscale radiometric pumps," Int. Commun. Heat Mass Transfer **121**, 105061 (2021).
[18] A. Lotfian and E. Roohi, "Species separation induced by difference in accommodation coefficients," Int. Commun. Heat Mass Transfer **161**, 108524 (2025).
[19] F. Han, X. Wang, F. Zhao, S. Zhang, and Z. Zhang, "Numerical investigation of gas separation via thermally induced flows in ratchet-like patterned microchannels," Int. J. Therm. Sci. **172**, 107280 (2022).
[20] H. Sugimoto, "Experiment on the gas separation effect of the pump driven by the thermal edge flow," AIP Conf. Proc. **1084**, 1123–1128 (2008).
[21] V. Kosyanchuk, V. Kovalev, and A. Yakunchikov, "Multiscale modeling of a gas separation device based on effect of thermal transpiration in the membrane," Sep. Purif. Technol. **180**, 58–68 (2017).
[22] C. Cercignani and M. Lampis, "Kinetic models for gas-surface interactions," Transp. Theory Stat. Phys. **1**, 101–114 (1971).
[23] G. Bird, *Molecular Gas Dynamics and the Direct Simulation of Gas Flows, Clarendon* (Oxford University Press, 1994).
[24] W. Wagner, "A convergence proof for Bird's direct simulation Monte Carlo method for the Boltzmann equation," J. Stat. Phys. **66**, 1011–1044 (1992).
[25] A. Shoja-sani, E. Roohi, M. Javani, H. Akhlaghi, and S. Stefanov, "Efficient collision algorithms in DSMC for rarefied gas dynamics: Markovian NTC-prescan and Bernoulli-trial schemes," Vacuum **247**, 115138 (2026).
[26] D. Ben-Adva, G. Tatsios, and A. Manela, "Kinetic description of flow detachment at a smooth micro-step: The near-free-molecular regime," Theor. Comput. Fluid Dyn. **39**, 11 (2025).